Simulation of electron beam lithography of nanostructures

M. Stepanova[a)]
National Institute for Nanotechnology NRC, 11421 Saskatchewan Drive, Edmonton, Alberta T6G 2M9, Canada

T. Fito, Zs. Szabó, and K. Alti
National Institute for Nanotechnology NRC, 11421 Saskatchewan Drive, Edmonton, Alberta T6G 2M9, Canada and Department of Electrical and Computer Engineering, University of Alberta, Edmonton, Alberta T6G 2V4, Canada

A. P. Adeyenuwo
Department of Electrical and Computer Engineeering, University of Alberta, Edmonton, Alberta T6G 2V4, Canada

K. Koshelev
National Institute for Nanotechnology NRC, 11421 Saskatchewan Drive, Edmonton, Alberta T6G 2M9, Canada and Department of Electrical and Computer Engineering, University of Alberta, Edmonton, Alberta T6G 2V4, Canada

M. Aktary
Applied Nanotools, Inc., 4465-99 Street, Edmonton, Alberta T6E 5B6, Canada

S. K. Dew
Department of Electrical and Computer Engineering, University of Alberta, Edmonton, Alberta T6G 2V4, Canada

(Received 8 July 2010; accepted 16 August 2010; published 1 December 2010)

The authors report a numeric simulation tool that they developed for the modeling and analysis of electron beam lithography (EBL) of nanostructures employing a popular positive tone resist polymethylmethacrylate (PMMA). Modeling and process design for EBL fabrication of 5–50 nm PMMA structures on solid substrates is the target purpose of the simulator. The simulator is functional for exposure energies from 1 to 50 keV with arbitrary writing geometries. The authors employ a suite of kinetic models for the traveling of primary, secondary, and backscattered electrons in the resist, compute three-dimensional (3D) distributions of the yield of main-chain scission in PMMA, and convert these into the local volume fractions of fragments of various sizes. The kinetic process of development is described by the movement of the resist-developer interface with the rate derived from the mean-field theory of polymer diffusion. The EBL simulator allows the computation of detailed 3D distributions of the yield of main-chain scission in PMMA for various conditions of exposure, the corresponding volume fractions of small fragments, and the clearance profiles as functions of the development in time and temperature. This article describes the models employed to simulate the EBL exposure and development, reports examples of the computations, and presents comparisons of the predicted development profiles with experimental cross-sectional resist profiles in dense gratings. © *2010 American Vacuum Society.* [DOI: 10.1116/1.3497019]

I. INTRODUCTION

Electron beam lithography (EBL) is a well-established core tool in the field of nanofabrication as it offers high flexibility and nanoscale resolution. Nonetheless, it remains a complex and sensitive process, particularly at dimensions approaching 10 nm and below. The use of modeling and simulation to develop a detailed understanding and rational optimization of EBL has been pursued for more than 4 decades. Published modeling studies address extensively the processes of electron penetration, scattering, and energy deposition in the resist and substrate materials by the Monte Carlo simulations[1–12] and kinetic transport theory.[13–20] In particular, elastic scattering of electrons traveling in the resist and backscattering from the substrate have been very well studied. The understanding of inelastic interaction of electrons with polymeric resists, although not yet complete, is generally considered sufficient for basic modeling of resist exposures by electrons. Particularly, computations of the spatial distributions of deposited energy in the exposed resist have been well represented.[1,6,8,10,13,15,16,18,20,21] However, obtaining a depiction of the final resist structure further involves accurately capturing the process of subsequent development. For positive tone polymeric resists, we feel models of EBL must go further to describe scission of the polymer chains, and kinetically treat the dissolution of fragments in the developer as a function of the scission fragment size. Unfortunately, the straightforward approach of using the distributions of deposited energy as a starting point for the computations of the number of scission leads to significant limitations. This is

[a)]Author to whom correspondence should be addressed; electronic mail: maria.stepanova@nrc-cnrc.gc.ca

because part of the deposited energy is thermalized without scissions involved and because the actual yield of scissions is related intimately with the details of individual collisions of electrons with the molecules of the resist. When all inelastic collisions occurring at a given location are represented simply by the total amount of deposited energy, the information on the individual collisions is lost. A solution that has been employed in most previous studies involves a conversion of the spatial distributions of deposited energy into the probability of bond scissions employing the empirical radiation chemical yield (G-factor), which is the number of main-chain scissions per 100 eV of deposited energy.[1,3,20,22,23] Usually, the G-factor is determined from experiments where the resist is exposed to extremely high energy (1 MeV regimes) electrons or gamma-rays.[24] Clearly, such experimental conditions differ dramatically from those employed in EBL, potentially invoking different physical process and presenting challenges to the applicability of scaling. We also showed[25] that the G-factor is not necessarily a constant, but may depend on the energies of electrons involved in collisions, and this dependence should be accounted for. To describe the EBL process at the deep nanoscale dimensions that are required by quickly progressing nanotechnologies, the approach to model exposure needs an improvement.

Another challenge in modeling EBL with positive tone resists is that the kinetic process of resist dissolution should be described. However, the dissolution of polymeric resists, such as polymethylmethacrylate (PMMA), is an extremely complex process; not all fundamental aspects of which have been understood sufficiently.[26–28] The framework adopted in most available simulations assumes an asymptotically stationary regime described by a constant rate of dissolution.[22,23,29] In these models, the rate of shift of the resist-solvent interface during dissolution is a simple function of local conditions of fragmentation. Unfortunately, this approach is not applicable in general. Thus, it excludes the classic Fickian regime that occurs in dissolution by diffusion.[30–32] Furthermore, the largely heuristic nature of such dissolution models challenges the understanding of underlying molecular mechanisms, as well as connecting the model parameters to basic kinetic and statistical-mechanical principles. In order to strengthen the predictive power of modeling at the nanoscale, and facilitate its further improvement, a more rigorous framework is required to describe the dissolution and clearance of the positive tone polymeric resists.

Recently, we worked to improve the models of EBL exposure and development of positive tone resist[25,33,34] in order to make them applicable to the deep nanosize regimes and facilitate their parametrization through the multiscale modeling framework based on more detailed molecular-level mechanisms. For exposure, we introduced a model[25] that explores an alternative approach of direct computation of the probability of main-chain scissions for inelastic collisions.[35] By this, the uncertainties related to the conversion of the cumulative deposited energy into the number of scissions through the empirical radiation chemical yield are avoided. The challenge of reaching an efficient performance at various length scales was solved by employing kinetic models to describe the exposure of PMMA. For development, we employed a kinetic model that describes the shift of the resist-developer interface as a function of time,[33,34] which we derived from the mean-field theory of polymer diffusion.[36] This relationship with a rigorous theory of molecular mobility makes the model parameterizable in terms of basic kinetics and statistical-mechanical constants, which facilitate its further improvement.

In this article, we summarize the distinguishing features of our integrated model for the exposure and development of PMMA resist, outline the capabilities of the simulation tool that implements the model, and give examples of the simulations compared with that of the experiments. We also discuss future developments and applications of the model.

II. MODELS FOR EXPOSURE AND FRAGMENTATION OF PMMA

In order to achieve an efficient performance, the model of exposure adopted in this article employs a kinetic transport theory to determine the distribution of primary, secondary, and backscattered electrons.[25] The inelastic interactions of electrons of energy E with resist atoms are described with the differential cross-section,

$$\mu(E,\varepsilon) = \sum_i N_i c_i \sigma(E,\varepsilon,U_i), \tag{1}$$

where ε is the relative energy transfer, $\varepsilon = \Delta E/E$, $\sigma(E,\varepsilon,U_i)$ is the Gryzinski differential inelastic cross-section,[25] N_i is the number density of shell electrons with the binding energy U_i, and c_i is an energy-dependent weight factor (employed for valence electrons only). The interactions with all valence electrons and with $1s$ electrons in O and C atoms in PMMA are accounted for. Following the approach introduced by Everhart and co-authors,[2,5] binding energies for core-shell electrons were taken from the literature, whereas those for valence electrons were described by an average binding energy $\bar{U}$. The resulting inelastic stopping power, expressed by

$$S(E) = E\int \mu(E,\varepsilon)\varepsilon d\varepsilon, \tag{2}$$

has been validated against the results of the dielectric response theory.[37] Agreement has been reached by employing the energy-dependent average binding energy $\bar{U}$ and weight factor c.[25]

As the next step, the spatial distribution of scission events in a planar layer of PMMA exposed to a point beam of primary electrons is computed. The geometric framework adopted for this follows the conventional approach as outlined, for example, in Ref. 35. First, the generation and transport of secondary, tertiary, and higher electrons, produced by a thin beam of primary electrons with energy E_P moving along a given direction, are described by the Boltzmann transport equation with sources and sinks given by collision integrals representing the inelastic collisions.[25] The latter are

described by the cross-section (1) parametrized as outlined above. Iterative numerical solution of the Boltzmann equation produces a distribution function of secondary electrons moving with energy E at a distance ρ from the primary beam, $f_S(E_p,\rho,E)$. The entire model system comprising both the primary beam and the secondary electrons is given by the distribution function,

$$f(E_p,\rho,E)=f_p\delta(\rho)\delta(E-E_P)+f_S(E_p,\rho,E), \tag{3}$$

where f_p is a flux constant and δ is the Dirac delta function. Equation (3) is further employed to compute the corresponding rate of scissions of the C–C bonds in the main-chain in PMMA,

$$Y(E_p,\rho)=\int f(E_P,\rho,E)\upsilon\mu_{\mathrm{C-C}}^{\mathrm{tot}}(E)dE, \tag{4}$$

where υ is the electron velocity and $\mu_{\mathrm{C-C}}^{\mathrm{tot}}$ is the total cross-section of inelastic collisions with valence electrons involved in backbone C–C bonds in PMMA. We define this cross-section by $\mu_{\mathrm{C-C}}^{\mathrm{tot}}(E)=w_{\mathrm{C-C}}c\int\mu_{\mathrm{valence}}(E,\varepsilon,U_{\mathrm{C-C}})d\varepsilon$. Here $\mu_{\mathrm{valence}}(E,\varepsilon,U_{\mathrm{C-C}})$ is the Gryzinski inelastic cross-section for valence electrons, where the average binding energy $\bar{U}$ is replaced with the main-chain dissociation energy $U_{\mathrm{C-C}}\approx 3.3$ eV, and $w_{\mathrm{C-C}}$ is the relative number of valence electrons involved in the main-chain C–C bonds. Further details can be found in Ref. 25. Finally, the radial distribution of the rate of scission, $Y(E_p,\rho)$, is converted into the corresponding average number of scissions per monomer, per electron, which is denoted as the yield of scissions, $w(E_p,\rho)$, in conventional EBL-applicable regimes $w(E_p,\rho)<1$; thus the yield w can also be interpreted as the probability of the main-chain scission.

As the next step, broadening and energy loss of primary electron beam is accounted for, in which the framework outlined in Ref. 35 has been employed. Based on the well-known kinematic arguments (see, e.g., Secs. IIA and IIB in Ref. 25), the model of the propagation of primary electrons has been factorized in such a way that inelastic collisions decrease the energy of primary electrons according to the stopping power from Eq. (2), whereas elastic collisions change only the direction of motion of the electrons, but not their energy. Broadening of the primary electron beam is described through the classic diffusion approximation.[15,16,18,19] For a point source of primary electrons traveling a distance in z, the lateral broadening is given by

$$P_P(\rho,z)\rho d\rho=\frac{3\lambda}{(z_{\max}-z)^3}\exp\left(-\frac{3\lambda\rho^2}{2(z_{\max}-z)^3}\right)\rho d\rho, \tag{5}$$

where z is the depth ($z=0$ corresponds to the bottom of the resist interfacing the substrate), $z_{\max}$ is the thickness of the resist, $z_{\max}-z$ is the distance from resist surface, and λ is the depth dependent elastic transport mean free path. The resulting depth distribution $P_P(\rho,z)$ is then convolved with the function $w(E_p,\rho)$, which produces a depth dependent radial distribution of the yield of scissions in a planar layer of PMMA exposed to the point electron beam, $w_P(\rho,z)$.

Finally, scissions by electrons backscattered from the substrate should also be accounted for. The backscattering coefficient and the distribution of backscattered electrons over the emission energy have been determined by the Staub model from Ref. 38 and validated against the experiment.[25] For the distribution of backscattered electrons over the emission angle θ, we employed the dependence $\cos(\theta)$, which is in reasonable agreement with numerical and experimental results reported in the literature.[17,39] The spread of the emission points is given by the following well-known distribution:

$$P_B(\rho)\rho d\rho=\frac{2}{\sigma^2}\exp\left(-\frac{\rho^2}{\sigma^2}\right)\rho d\rho. \tag{6}$$

Here, ρ is the distance relative to the impact point of the primary electron, and $\sigma(\mathrm{nm})=4.52\times10^3 r^{-1}(E_{P_s}/2\cdot10^4)^{1.65}$, where r is density of the substrate in g/cm^3 and E_{P_s} is the energy of the primary electrons (in eV) when they reach the substrate. To describe the emission of backscattered electrons, the function $P_B(\rho)$ is convolved with the distribution of primary electrons at the bottom of the resist, $P_P(\rho,0)$. Propagation of backscattered electrons in the resist, generation of the corresponding secondary electrons, and the chain scissions are handled following the framework described above, producing a depth dependent radial distribution of the yield of main-chain scissions by backscattered electrons, $w_B(\rho,z)$.

Adding together the local yields of scissions generated by forward and backscattered electrons, $w_P(\rho,z)$ and $w_B(\rho,z)$, provides the total depth dependent radial distribution of the scissions of the main-chain in a planar layer of PMMA exposed by the point beam, $w(\rho,z)=w_P(\rho,z)+w_B(\rho,z)$. This distribution replaces the conventional point spread function (PSF); however, as distinct from the PSF for deposited energy, our yield of scissions is computed directly from inelastic collision events by primary, secondary, and backscattered electrons. The corresponding cross-sections are intimately related to the molecular mechanisms involved, allowing for clearer interpretations and more direct paths toward further improvement of the model. Also, the usage of the kinetic approaches to compute the function $w(\rho,z)$ favorably affects the efficiency of the approach compared with the direct Monte Carlo simulations, particularly when computing the contribution from backscattered electrons, $w_B(\rho,z)$, at the same time allowing for a nanoscale resolution for the contribution from the forward beam, $w_P(\rho,z)$.

The next step is a convolution of the radial distribution of the yield of scissions from a point beam $w(\rho,z)$ with the writing pattern in the lateral plane $\{x,y\}$, which results in a three-dimensional (3D) spatial distribution of the yield of scission per PMMA monomer, $W(x,y,z)$. For the following analysis, the probability of bond scissions rather than the average number of scissions per bond is required. For this reason, the distribution $W(x,y,z)$ has been truncated at the level of 1 at locations where higher average numbers of

scission per bond have occurred, so that $W(x,y,z) \leq 1$.[40] The truncated value W is referred to as the probability of scissions.

Assuming that the probability of bond scission does not depend on bond position in the PMMA chain and on its length, the distribution of polymer chain length after the scission process can be found, which depends on $W(x,y,z)$ and the initial number of monomers in a resist molecule, n_{init}. At the condition $n_{\text{init}}W \gg 1$, which is satisfied for $n_{\text{init}}=9600$, the geometrical distribution is applicable.[41–43] The corresponding probability to find a fragment containing n monomers at a given location $\{x,y,z\}$ is expressed by

$$C_n(x,y,z) = W(x,y,z)(1 - W(x,y,z))^{n-1}, \tag{7}$$

and the volume fraction of fragments containing n monomers is found to be

$$\varphi_n(x,y,z) = \frac{nC_n(x,y,z)}{\sum_{n=1}^{\infty} nC_n(x,y,z)} = nW^2(x,y,z)(1 - W(x,y,z))^{n-1}. \tag{8}$$

In Sec. III, we describe a model of development of exposed PMMA, assuming that the 3D distribution of local volume fractions of fragments is known.

III. KINETIC MODEL FOR RESIST DEVELOPMENT

As a background for our models of resist development, we employed the recent mean-field theory of diffusion in polymeric systems.[36] The theory accounts for the molecular mobility, intermolecular interactions, and pressure relaxation in a system containing a solvent and polymer chains of various lengths. Although the original work[36] addresses only the stationary-state boundary conditions, the theory is readily extensible to more general nonstationary behaviors.[34] After the extension to the nonstationary case, general time dependent equations of the mean-field theory describe the volume fraction of the components, $\varphi_i(r,t)$, as a function of the location r and time t, where i denotes different molecules.[34] With appropriate initial and boundary conditions, the numeric solution of the general mean-field equations[34,36] would predict dissolution of exposed PMMA as a function of time. This, however, would require defining all parameters in the general model, which include the diffusivities D_i and the Flory–Huggins (FH) interaction parameters χ_{ik} for all components in the system, which is a tremendously complex task. Also, the numeric solution of the full system containing PMMA fragments of various sizes and the developer is a very time-consuming process, whereas a high computational efficiency is required for insilico aided optimization of the EBL process. For these reasons, we employed the model,[36] extended to the nonstationary case,[34] as a starting point to derive a simpler, but more efficient model that describes the kinetic process of development by the movement of the resist-developer interface, and contains less unknown parameters.[33,34,43] In brief, we consider the exposed PMMA resist embedded in a developer (solvent) and denote the developer by index 0 and PMMA fragments by index $n>0$, corresponding to n monomer units. Further, we define the position of the resist-developer interface, $\mathbf{r}_{\text{int}}$, as the level surface of equal developer concentration, $\varphi_0(\mathbf{r}_{\text{int}},t)=p=\text{const}$. Next, we introduce the velocity at which the interface changes its position, $\mathbf{v}=d\mathbf{r}_{\text{int}}/dt$,

$$\mathbf{v} \cdot \nabla \varphi_0|_{\mathbf{r}=\mathbf{r}_{\text{int}}(t)} = \nabla \mathbf{J}_0|_{\mathbf{r}=\mathbf{r}_{\text{int}}(t)}, \tag{9}$$

where $\mathbf{J}$ is the flux generated by the local gradient of the chemical potential.[34,36] The resist shrinks at the condition $\nabla \mathbf{J}_0 < 0$ and swells otherwise. Expecting that the swelling of the resist would prevail only at the beginning of dissolution, whereas shrinking is the major mechanism responsible for development, we have focused our analysis on the shrinking regime.

We assume that there is no interaction between the polymer chains, so that $\chi_{nk}=0$ for $n, k>0$, and that the interaction with the developer does not depend on the size of PMMA fragments, $\chi_{n0}=\chi_{0n}=\chi$. We also require miscibility of PMMA with the developer, which implies the condition $1-2\chi>0$. Further to this, we consider a model condition when at every location, the polymer is represented by one characteristic size of fragments n and also account for the fact that usually $D_0 \gg D_n$. It is possible to demonstrate[43] that with these definitions and assumptions, the expression for the velocity of motion of the resist-developer interface v can be asymptotically evaluated by

$$v(\mathbf{r}_{\text{int}}) = \frac{\eta D_n(\mathbf{r}_{\text{int}})}{L}. \tag{10}$$

Here, L represents the depth of shrinkage, $D_n(\mathbf{r}_{\text{int}})$ is the diffusivity of PMMA at location $\mathbf{r}_{\text{int}}$, and η is a constant coefficient that depends on the FH parameter χ and on the function $\varphi_0(l)$, where l is the coordinate across the solvent-polymer interface. For example, if the function φ_0 decays asymptotically as $\varphi_0=a/l$ then $\eta=2a(1-p)(1-2\chi)$. A more general case is considered in Ref. 43. One can further describe the kinetics of resist dissolution by

$$\frac{dL}{dt} = \frac{\tilde{D}_n(\mathbf{r}_{\text{int}})}{L}, \tag{11}$$

where $\tilde{D}_n$ is the effective local diffusivity, $\tilde{D}_n=\eta D_n$. In a case of homogeneous diffusivity $\tilde{D}_n$, the integration of Eq. (11) provides the well-known expression of the Fickian diffusion length,[30,32] $L \sim (D_n t)^{1/2}$, and for the corresponding rate of resist dissolution, one obtains $v \sim (D_n/t)^{1/2}$. An important implication is that the rate of resist dissolution v is a function of the entire history of the process of development, and not asymptotically a constant as hypothesized in most other models of EBL resist dissolution.[22,23,29] Our analysis demonstrates that the last assumption is not applicable in general, and that a more complex kinetics of dissolution should be accounted for to describe the resist development at the nanoscale.

For the normalized diffusivity of fragments of the size n, we employ the expression[26,27]

$$\tilde{D}_n = n^{-\alpha}\beta(T), \tag{12}$$

where the factor $\beta(T)=b\exp(-U/kT)$ accounts for the temperature dependence of the diffusivity, and that $n^{-\alpha}$ can be interpreted as describing the decrease of the mobility of polymer fragments with their size n.[27] The theory of molecular liquids[44] predicts that power α can vary from 1 in diluted solution or in polymer melt consisting only of small fragments (the Rouse regime) to 2 for longer fragments in dense polymer melts (the entanglement regime). Recently, these predictions have been confirmed by molecular dynamics simulations, which also demonstrated that in the entanglement regime, the power α can reach 2.4.[45]

Since in exposed PMMA, fragments with various sizes are represented by a distribution $\varphi_n(x,y,z)$, the location dependent average effective diffusivity can be computed as

$$D(x,y,z) = \langle \tilde{D}_n \rangle = \left\langle \frac{\beta(T)}{n^{\alpha(x,y,z)}} \right\rangle, \quad \alpha(x,y,z) = \begin{cases} 1+\langle n\rangle/n_0, & \langle n\rangle < n_0 \\ 2, & \langle n\rangle \geq n_0, \end{cases} \tag{13}$$

where averaging is performed over the local size distribution of fragments, and the parameter n_0 represents a characteristic fragment size at which the entanglement regime is reached.

The parameters employed to describe the development comprise the activation energy U, the effective diffusion preexponential factor b, and the characteristic fragment size for the entanglement regime n_0. In the present work, the model parameters U, b, and n_0 have been evaluated by fitting the computed percentages of PMMA left on the substrate to the corresponding experimental results.[43] We used scanning electron microscopy (SEM) cross-sectional images for periodic gratings in 950 K PMMA exposed with a RAITH150 EBL instrument with 10 keV voltage and developed in a 3:1 isopropanol: methyl-isobutylketone (IPA:MIBK) solution at various times and temperatures from −15 °C to room temperature. The experimental procedure employed to fabricate the gratings and obtain the SEM images for comparison with the simulations can be found in Refs. 33, 34, and 46. It has been found that for PMMA developed in the IPA:MIBK solution, the activation energy $U=0.56$ eV and the preexponential factor $b=1.5\times10^{14}$ nm^2/s may be used. A temperature independent value of $n_0=17$ has also been identified. The methodology employed for data fitting is described elsewhere.[43]

In distinction of most existing simulation approaches, in our model the parameters describing the resist dissolution are decoupled from those describing the chain scission. As a result, all parameters in our model of development are basic kinetic and statistical-mechanical quantities and related directly to theoretical frameworks employed in molecular theory of liquids. Consequently, our model adopts a multiscale bottom-up parametrization in principle. The intense progress occurring in the theory of molecular liquids raises expectations that the multiscale bottom-up modeling of development based on fundamental molecular mechanisms may be available soon to replace the empirical parametrization.

IV. SIMULATION OF NANOSCALE EBL

Employing the models of exposure and development discussed in Secs. II and III, we have created a simulation tool intended to predict and analyze the outcome of EBL of nanostructures sized down to 1–5 nm. A detailed description of the programming implementation of the simulator is not the objective of this article, and thus only a brief technical outline is given. The simulator is written using MICROSOFT VISUAL STUDIO (PROFESSIONAL) 2005 employing OpenGL for plotting the results, and compiled for WINDOWS XP and WINDOWS 7. The simulator provides 3D distributions with a 1 nm resolution for the scission, fragmentation, diffusivity, and clearance profiles in the resist. Arbitrary exposure geometries, either individual or periodic, are supported. Simple writing geometries, such as single-pixel dots, lines, rectangular structures, or periodic grating patterns composed of such structures, can be specified through a graphical user interface (GUI). For more complex patterns, import of grayscale graphical images is available employing 255 levels of gray to map the exposure dose distribution. Due to the graphical import, the simulator handles arbitrary writing patterns, either individual or periodic.

The current version of the simulator supports the exposure voltage regimes from 1 to 50 keV, employing a PMMA resist on conducting substrates. After input of initial conditions, such as the thickness of PMMA, substrate material data, writing pattern, exposure voltage, and exposure dose level(s), a 3D distribution of the yield of the main-chain scission per monomer, $W(x,y,z)$, is computed by a convolution of the writing dose pattern with the scission yield function of a single-pixel beam, $w(x,y,z)$. The single pixel beam width is 2 nm, and the step size of the beam may be varied. Figure 1(a) shows an example of a writing pattern in a form of a grayscale image where the levels of gray determine the point exposure dose applied, and Fig. 1(b) demonstrates the corresponding computed 3D distribution of the yield of scissions for a 20 keV exposure. For large writing patterns, it is possible to perform high-resolution computations in a selected smaller computational box. An example of a computational box selected in a larger image is shown by red lines in Fig. 1(a), and the corresponding computed 3D distribution of the yield of scission is presented in Fig. 1(c). Full accounting for all proximity effects from forward-scattered and backscattered electrons is done in the small-box computations. In the future, this feature can be employed to parallelize the computations in order to increase their efficiency for large writing patterns. After the 3D local yield of scission $W(x,y,z)$ is computed, these data can be converted into corresponding local distributions of PMMA fragments over their sizes, employing Eqs. (7) and (8). The simulator allows the computation of 3D dependencies of the volume fractions of small fragments with the number of monomers $n<n_{\max}$, where $n_{\max}$ can be varied.

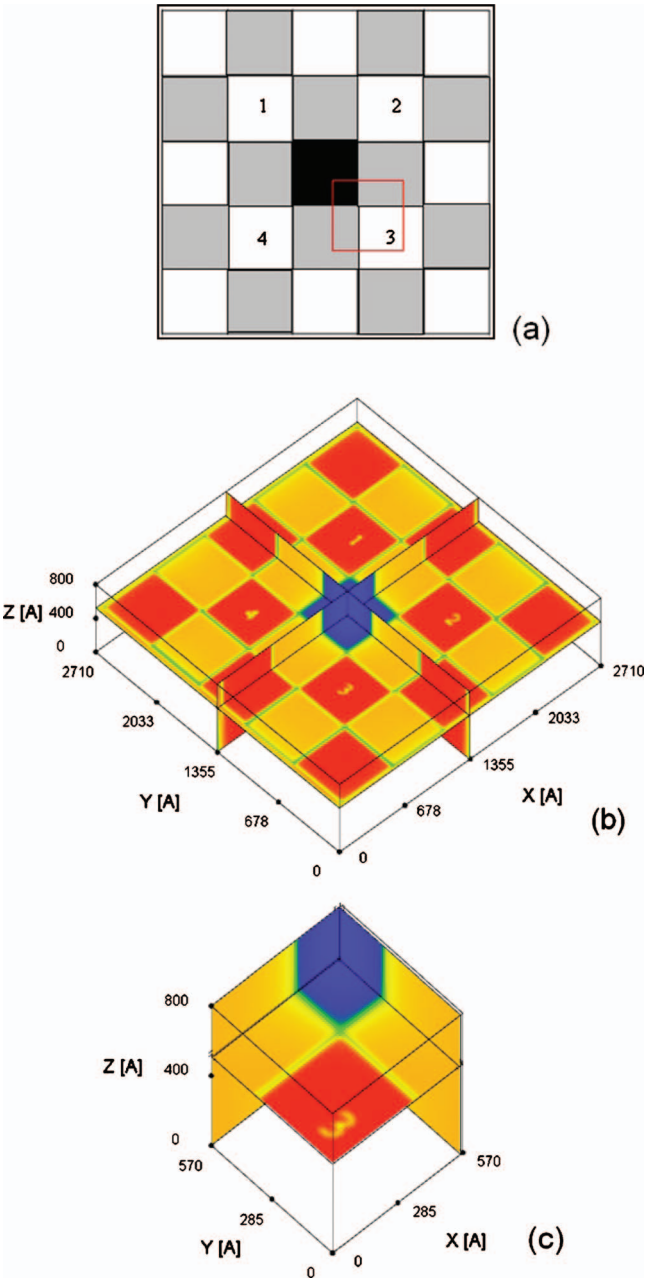

FIG. 1. (Color) (a) Example of an input writing pattern in a form of a grayscale image where the levels of gray determine the point exposure dose applied, (b) computed 3D distribution of the yield of scissions employing 20 keV exposure of a 80 nm layer of PMMA on a Si substrate, (c) 3D distribution of the yield of scission computed in a smaller box shown by red lines in (a). In (a), white color indicates the highest point doses applied, and black indicates no exposure. In (b) and (c), red and blue colors indicate the highest and the lowest level of the scission yields, respectively. The size labels along the axes in (b) and (c) are in Å.

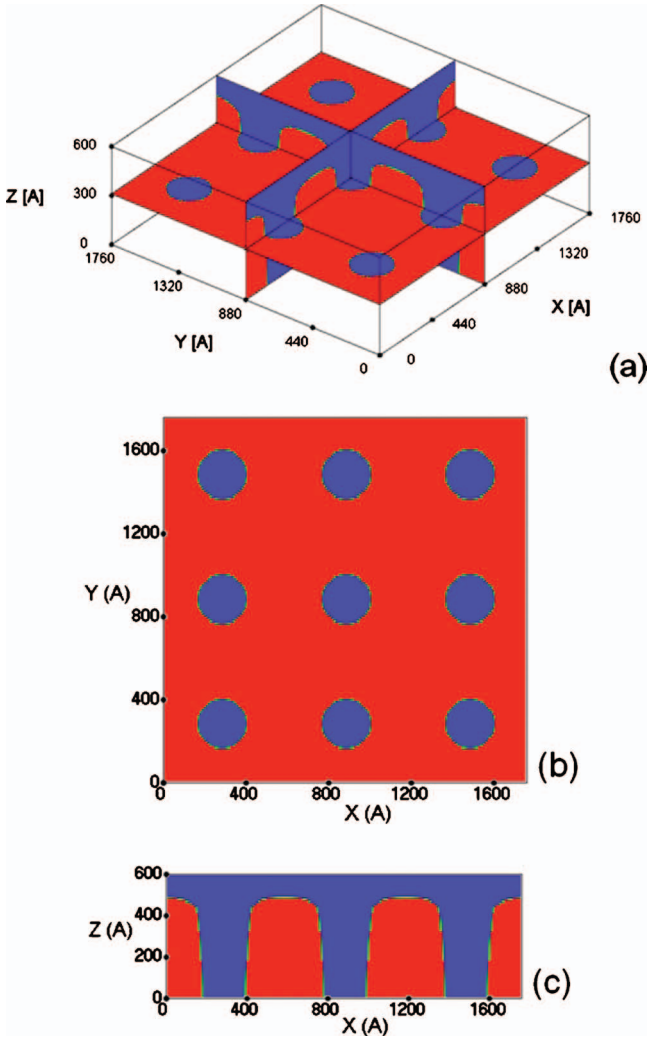

FIG. 2. (Color) (a) 3D development profile of a periodic pattern composed of single-pixel dots with a 60 nm pitch in an initially 60 nm thick layer of PMMA on a Si substrate, (b) 2D cross-section of the development profile in the $\{X,Y\}$ plane at 30 nm depth, (c) 2D cross-section in the $\{X,Z\}$ plane in the middle of the image. The dots were exposed with 50 keV and a point dose of 0.003 pC, and developed for 10 s at room temperature. Red color denotes undissolved PMMA, and blue color denotes clearance. In (a) and (c), the largest coordinate along the z-axis (60 nm) denotes the initial thickness of PMMA. The size labels along the axes are in Å.

Employing the computed scission and fragmentation data, the kinetic process of resist clearance can be modeled. For this purpose the conditions of development, comprising the time and temperature, should be inputted through the GUI. To simulate the development process expressed by Eqs. (10) and (11), the simulator implements a sequence of discrete dissolution steps with time δt required to dissolve a resist layer of thickness δL determined by $\delta t = 2L\delta L / D(x,y,z)$, where the effective local diffusivity $D(x,y,z)$ is given by Eq. (13). The simulation provides the location of the 3D resist-developer interface as a function of development time. Figure 2 demonstrates a development profile of a periodic pattern composed of single-pixel dots with a 60 nm pitch exposed with 50 keV voltage in a 60 nm thick layer of PMMA on a Si substrate, and developed at room temperature. Figure 2(a) shows the 3D development profile, and Figs. 2(b) and 2(c) display its two-dimensional (2D) cross-sections in the horizontal and vertical planes. In Figs. 2(a) and 2(c), the largest coordinate along the z-axis denotes the initial thickness of PMMA. In addition to the development profiles, it is also possible to output the 3D function $D(x,y,z)$.

V. RESULTS AND DISCUSSION

In this section, we present the selected results of our simulations of the development profiles and provide a comparison with that of the experiments. As a reference structure, we employed experimental SEM cross-sectional images of exposed and developed gratings in 950K PMMA, with the nominal initial thickness of 55 nm, on a Si substrate, which have been available from earlier works described in Refs. 33, 34, and 46. In all experiments, a 3:1 IPA:MIBK mixture was used as the developer. The simulations were performed employing the values of dissolution model parameters described in Sec. III.

Figure 3 presents a comparison of computed and experimental cross-sectional profiles in periodic grating structures exposed with 30 keV electrons and developed for 15 s at −15 °C temperature. Figures 3(a)–3(d) present gratings with pitches of 50 and 70 nm, respectively, fabricated with the same exposure dose of 2000 pC/cm.[47] Despite the similar dose applied, the simulated trenches are slightly wider in 50 nm pitch grating [Fig. 3(a)] than in 70 nm pitch grating [Fig. 3(c)]. The main reason of this is the impact of backscattered electrons, which is higher in a denser 50 nm pitch grating than in a 70 nm pitch grating. The other pair of figures, Figs. 3(e) and 3(f), show the same conditions as Figs. 3(c) and 3(d) except for a higher exposure dose, which is 4500 pC/cm. Overall, the computed resist profiles from Figs. 3(a), 3(c), and 3(e) agree reasonably with the experimental ones in Figs. 3(b), 3(d), and 3(f).

In Figs. 4(a)–4(d), simulated cross-sectional profiles of a 70 nm pitch grating exposed with 10 keV electrons and developed at room temperature during 5 s [Fig. 4(a)] and 20 s [Fig. 4(c)] are compared with the corresponding experiment, whereas in Figs. 5(a) and 5(b), a similar comparison is done for a grating exposed with 3 keV electrons. From the comparison of Figs. 4 and 5, it is evident that the 3 keV exposure requires almost twice a lower dose to reach clearance (150 pC/cm in this example) compared with the 10 keV exposure (271 pC/cm). The higher sensitivity of the low-keV exposures is a well-known fact related to the energy dependence of the interaction of electrons with the resist, which we thoroughly explored experimentally.[33,34] The comparison of computed and experimental resist profiles in Figs. 4 and 5 demonstrates that the simulator reproduces reasonably the observed voltage dependence of the resist sensitivity.

The comparison of the simulated profiles from Figs. 3(a), 3(c), 4(a), and 5(a) shows a trend of a relative increase in the trench width at the bottom of the resist, with an undercut clearly seen in the 3 keV profile [Fig. 5(a)]. The reason for this is the broadening of the primary beam due to forward scattering, which becomes stronger for low-keV exposures. Our analysis of the corresponding scission and fragmentation profiles has demonstrated that for thin PMMA films such as considered in these examples, broadening of the electron beam by forward scattering is insignificant for 30 keV exposures, increases somewhat for 10 keV exposures, and is strongly pronounced for 3 keV exposures. As a result, the simulations consistently predict undercuts for 3 keV exposures in 50–60 nm thick resists. The experimental cross-sectional profiles for the gratings exposed with 3 keV voltages and developed at room temperature [Fig. 5(b)] and at −15 °C (Ref. 33) confirm this trend.

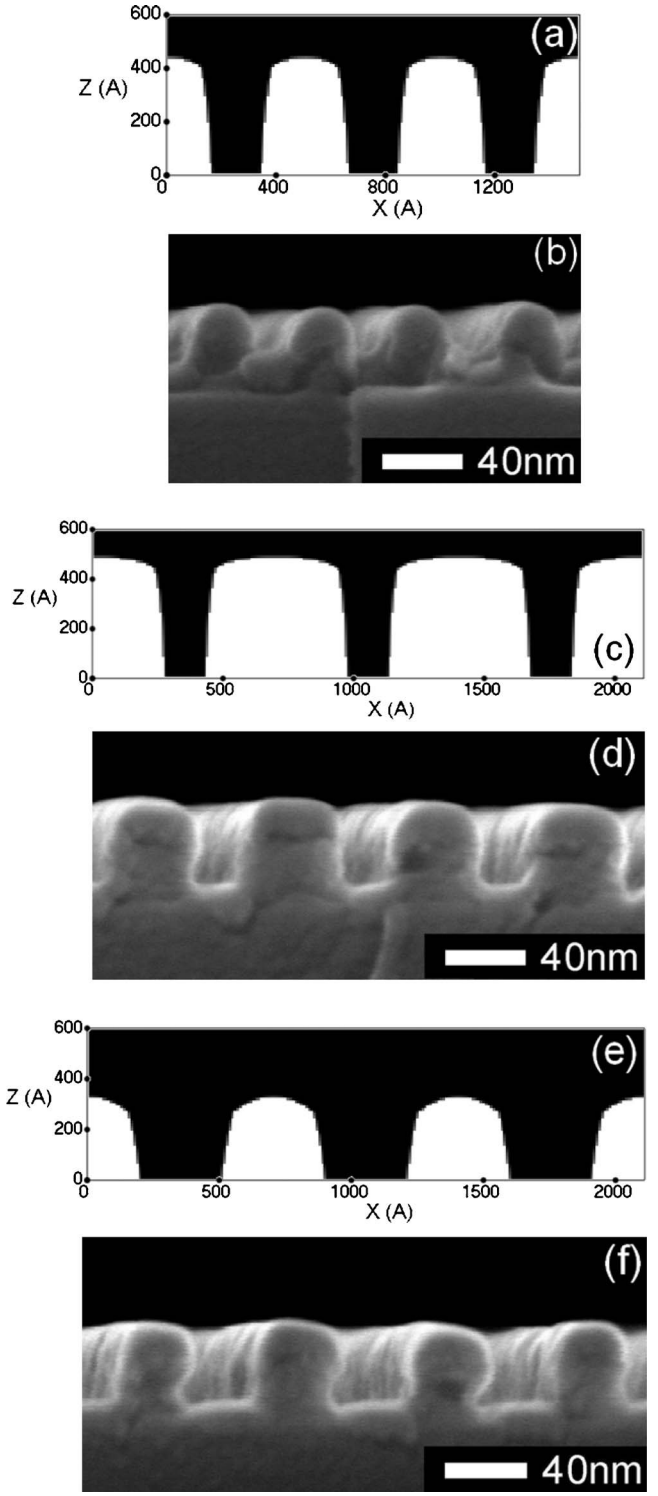

FIG. 3. Comparison of simulated [(a), (c), and (e)] and experimental [(b), (d), and (f)] cross-sectional profiles of gratings in PMMA on a Si substrate, exposed with a 30 keV voltage and developed in a 3:1 IPA:MIBK mixture during 15 s at −15 °C. [(a) and (b)] 50 nm pitch, [(c)–(f)] 70 nm pitch, [(a)–(d)] 2000 pC/cm line dose, [(e) and (f)] 4500 pC/cm line dose. In (a), (c), and (e), white denotes undissolved PMMA, and black denotes clearance.

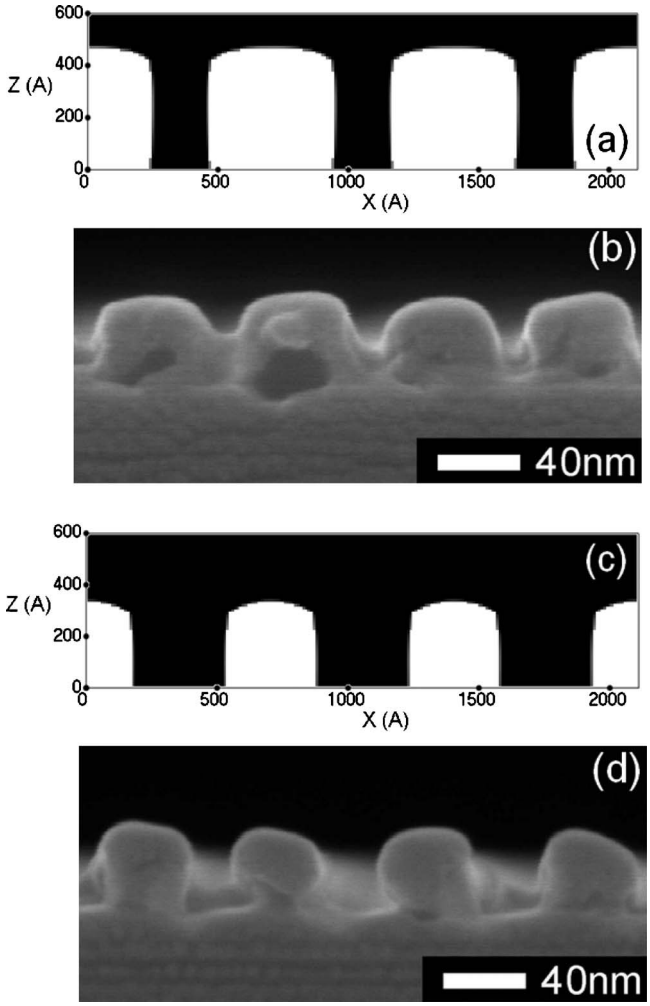

FIG. 4. Comparison of simulated [(a) and (c)] and experimental [(b) and (d)] cross-sectional profiles of 70 nm pitch gratings exposed with a 10 keV voltage and a 271 pC/cm line dose, and developed at room temperature for 5 s [(a) and (b)] and 20 s [(e) and (f)].

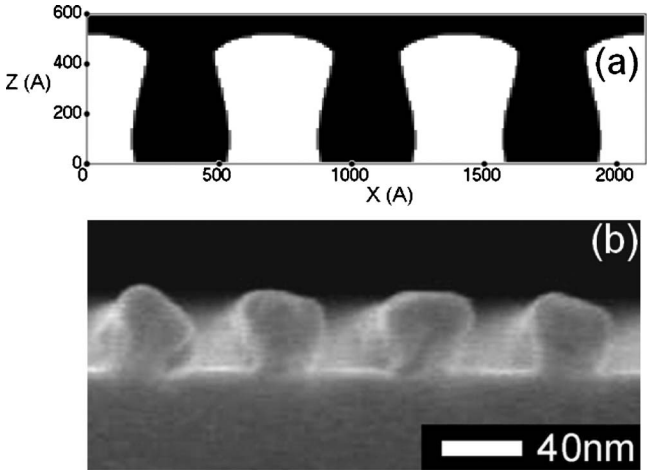

FIG. 5. Comparison of simulated (a) and experimental (b) cross-sectional profiles of 70 nm pitch gratings exposed with a 3 keV voltage and a 150 pC/cm (a) and 145 pC/cm (b) line dose, and developed at room temperature for 5 s.

As we demonstrated recently,[48] 3 keV exposures have a potential not only to provide a substantial improvement of the process throughout but also to facilitate application of EBL in fabricating nanosized masks by metallization. By employing 3 keV voltage exposures of PMMA, we were able to fabricate arrays of 15–20 nm wide metal (Cr) lines in a grating configuration with a 50 nm pitch, and also developed a highly efficient process for fabricating 16 nm wide bridge structures of a dielectric material.[48] The undercuts created by the ultralow energy exposures allowed us to use a single layer of PMMA avoiding the more complex bilayer schemes that are often used for lift-off at the deep nanoscale. This improvement, however, comes at the expense of the need to carefully select the appropriate exposure (dose) and development (temperature, duration) conditions.[34] For the purpose of such process optimization, detailed simulations of EBL, such as reported here, are particularly helpful. Speaking more generally, the three-dimensional shaping of resists by employing the broadening of the electron beam due to forward scattering is one of the possible applications of 3D simulations of resist clearance. It should be noted that ultralow-keV exposures are important, but not unique regime when a better understanding of 3D resist shaping is required. It is well-known that electron beams of any energy would undergo a broadening if the resist layer is thick enough. As an example, Figs. 6(a) and 6(b) present computed clearance profiles for grating structures in 40 nm thick PMMA exposed with 1 keV electrons, and in 300 nm thick PMMA exposed with 10 keV electrons. Both exhibit re-entrant profiles broadening from the top to bottom. Understanding how such profiles depend on EBL process conditions by employing a 3D modeling will facilitate the applications in emerging areas of nanomanufacturing, such as microfluidics and photonics.

Another important application of the detailed numeric modeling of 3D resist profiles is to complement experimental studies by predicting basic trends of the EBL process, which may further be employed to predetermine the process conditions for further refinement. Figure 7 presents a set of computed cross-sectional profiles in a grating with a 70 nm pitch, exposed with 10 keV voltage and the doses of 300, 600, 1200, and 2400 pC/cm, and developed during 0.5, 2, 8, and 32 s at −15 °C. The profiles show a broad range of conditions of clearance, from strongly underdeveloped to entirely cleared. Interestingly, some of the profiles appear to be close in width of the trench despite the different process conditions. Figure 8(a) presents the widths of the developed trenches Δx, measured at the half-depth of the trench, for various line doses and development times, including those shown in Fig. 7. It is clearly seen that the dependence of Δx on the value $dt^{1/2}$, where d is the exposure dose and t is development time, is very close to linear. Figure 8(b) presents a similar dependence for 30 keV exposures, which exhibit a compatible trend. The existence of such a linear dependence, relating the width of trench, exposure dose, and development time, is not surprising considering that in our model, removal of the resist is associated with the diffusion length of PMMA fragments $(Dt)^{1/2}$, where the effective dif-

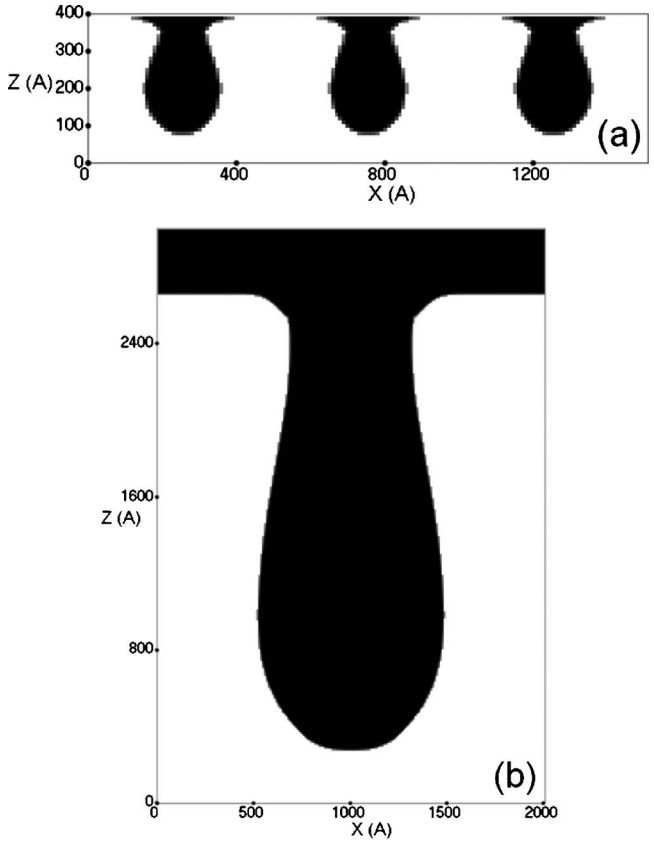

FIG. 6. Examples of computed reentrant resist profiles with undercuts created by forward scattering of electrons: (a) a grating in a 40 nm thick layer of PMMA exposed with 1 keV voltage and (b) a grating in a 300 nm thick layer of PMMA exposed with 10 keV voltage. White denotes undissolved PMMA, and black denotes clearance. The size labels along the axes are in Å.

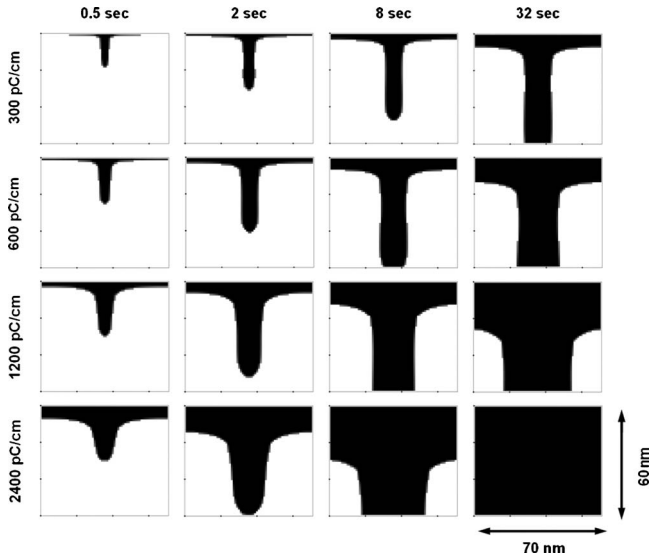

FIG. 7. Computed clearance profiles in a periodic grating with a 70 nm pitch exposed with 10 keV voltages with various doses, and developed at −15 °C and various durations. The width of all boxed is 70 nm, and the height is 60 nm. The ticks on the axes indicate 20 nm intervals. White denotes undissolved PMMA, and black denotes clearance.

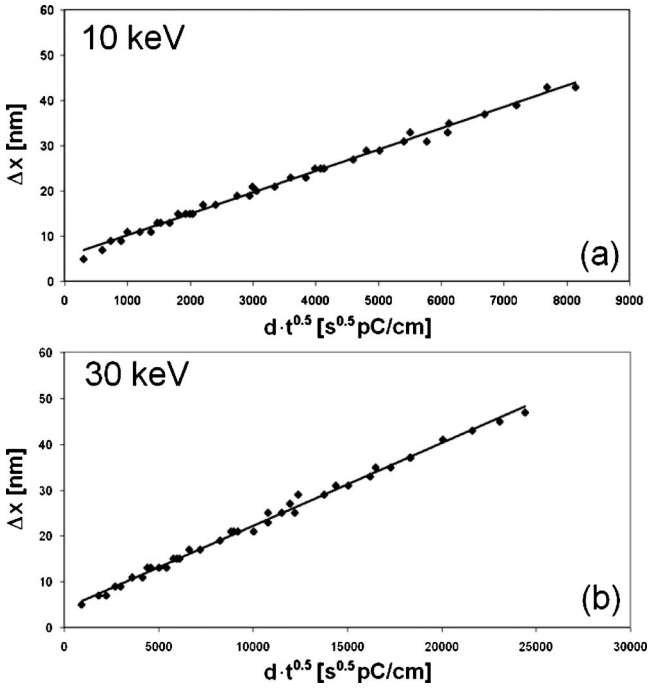

FIG. 8. Scaling dependencies relating the width of developed trenches measured at the half-depth of the trench, with the exposure dose d and development time t, determined from simulations for periodic 70 nm gratings in a 60 nm thick PMMA, exposed with 10 keV (a) and 30 keV (b) voltages, and developed at −15 °C.

fusivity D is given by Eq. (13), and also can be approximately represented by a proportionality $D \sim d^2\beta(T)$.[33,46] Here, $\beta(T)$ is the temperature dependent coefficient from Eq. (13) and d is the dose.[33,46] Accordingly, one may expect that the width of clearance trenches can be asymptotically evaluated by a linear dependence

$$\Delta x = A + Bd\beta(T) \cdot t^{1/2}, \tag{14}$$

where A and B are constants in the time and dose regimes considered. If confirmed to be sufficiently universal, scaling laws like this may be employed for the fast evaluation of desired EBL process conditions. The small offset A reflects the fact that the linear dependence does not apply at low exposure doses or very short development times. It also should be noted that the linear scaling law originates from the Fickian character of the dissolution model in Eqs. (10) and (11), which is employed in the present simulation. Other models of dissolution may result in a different scaling dependence. One can expect that future experimental investigations of the scaling laws of clearance in various resist-developer pairs, complemented by modeling studies, would be capable to tell whether a universal development mechanism may de identified to describe the kinetics of clearance for various positive tone resists and developer formulas.

VI. CONCLUSION

We have presented an improved simulation framework for modeling electron beam fragmentation and developing positive tone resists, implemented it in a flexible simulation tool,

and described examples of applications to EBL fabrication of nanostructures using PMMA as the resist. The numerical results agree reasonably with available experiments, and also allow interpreting and systematizing the observed trends. This is particularly important considering the challenging task of co-optimizing at least four process parameters (the exposure voltage, dose, development temperature, and time) that are often required to reach deep nanoscale resolution with the EBL process. Understanding the complex interrelation of the different factors influencing the outcomes of EBL is facilitated significantly by the simulations. Furthermore, the efficient simulation tool offers a strong potential for computer-aided optimization of electron beam lithography.

The kinetic and statistical-mechanical approaches employed make the simulator efficient enough at the nanometer size scales, which is an important capability in view of the emerging molecular-level processes of nanomanufacturing. The framework employed also potentially allows for further extensions of the model to include a broader range of physicochemical processes accompanying the resist dissolution, such as phase separation and swelling, whose potential impact on the performance of the process is not yet understood sufficiently. Further effort should also address strengthening the predictive capacity of the kinetic models by a bottom-up multiscale parameterization, employing more detailed molecular simulations at the background.

ACKNOWLEDGMENTS

The authors would like to thank Jiang Chen for preparing the experimental samples and making the cross-sectional SEM images that were used in this work. The work was supported by NINT-NRC, NSERC, Alberta Advanced Education and Technology (AAE&T), iCORE, and Raith GmbH.

[1]D. F. Kyser and N. S. Viswanathan, J. Vac. Sci. Technol. **12**, 1305 (1975).
[2]R. Shimizu and T. E. Everhart, Appl. Phys. Lett. **33**, 784 (1978).
[3]M. Parikh and D. F. Kyser, J. Appl. Phys. **50**, 1104 (1979).
[4]D. F. Kyser and R. Ryle, IBM J. Res. Dev. **24**, 426 (1980).
[5]I. Adesida, R. Shimizu, and T. E. Everhart, J. Appl. Phys. **51**, 5962 (1980).
[6]K. Murata, D. F. Kyser, and C. H. Ting, J. Appl. Phys. **52**, 4396 (1981).
[7]N. Samoto and R. Shimizu, J. Appl. Phys. **54**, 3855 (1983).
[8]K. Murata, H. Kawata, K. Nagami, Y. Hirai, and Y. Mano, J. Vac. Sci. Technol. B **5**, 124 (1987).
[9]C. R. K. Marrian, F. K. Perkins, D. Park, E. A. Dobisz, M. C. Peckerar, K.-W. Rhee, and R. Bass, J. Vac. Sci. Technol. B **14**, 3864 (1996).
[10]S.-H. Kim, Y.-M. Ham, W. Lee, and K. Chun, Microelectron. Eng. **41–42**, 179 (1998).
[11]Y. Lee, W. Lee, K. Chun, and H. Kim, J. Vac. Sci. Technol. B **17**, 2903 (1999).
[12]V. V. Ivin, M. V. Silakov, G. A. Babushkin, B. Lu, P. J. Mangat, K. J. Nordquist, and D. J. Resnik, Scanning **11**, 176 (1989).
[13]J. S. Greeneich and T. Van Duzer, IEEE Trans. Electron Devices **21**, 286 (1974).
[14]T. Biewer and P. Rez, J. Appl. Phys. **76**, 7636 (1994).
[15]N. Glezos, I. Raptis, D. Tsoukalas, and M. Hatzakis, J. Vac. Sci. Technol. B **10**, 2606 (1992).
[16]I. Raptis, N. Glezos, and M. Hatzakis, J. Vac. Sci. Technol. B **11**, 2754 (1993).
[17]H. Schmoranzer and M. Reisser, Nucl. Instrum. Methods Phys. Res. B **105**, 35 (1995).
[18]N. Glezos and I. Raptis, IEEE Trans. Comput.-Aided Des. **15**, 92 (1996).
[19]B. K. Paul, Microelectron. Eng. **49**, 233 (1999).
[20]I. Raptis, N. Glezos, E. Valamontes, E. Zervas, and P. Argitis, Vacuum **62**, 263 (2001).
[21]J. Zhou and X. Yang, J. Vac. Sci. Technol. B **24**, 1202 (2006).
[22]J. S. Greeneich, J. Vac. Sci. Technol. **12**, 5264 (1974).
[23]G. Han, M. Khan, and F. Cerrina, J. Vac. Sci. Technol. B **21**, 3166 (2003).
[24]A. Chapiro, *Radiation Chemistry of Polymeric Systems* (Wiley, New York, 1962), p. 515.
[25]M. Aktary, M. Stepanova, and S. K. Dew, J. Vac. Sci. Technol. B **24**, 768 (2006).
[26]L. Masaro and X. X. Zhu, Prog. Polym. Sci. **24**, 731 (1999).
[27]B. A. Miller-Chou and J. L. Koenig, Prog. Polym. Sci. **28**, 1223 (2003).
[28]D. Achilias, Macromol. Theory Simul. **16**, 319 (2007).
[29]D. G. Hasko, S. Yasin, and A. Mumatz, J. Vac. Sci. Technol. B **18**, 3441 (2000).
[30]F. Brochard and P. G. de Gennes, Europhys. Lett. **1**, 221 (1986).
[31]J. S. Papanu, D. S. Soane, A. T. Bell, and D. W. Hess, J. Appl. Polym. Sci. **38**, 859 (1989).
[32]B. Narasimhan and N. A. Peppas, Adv. Polym. Sci. **128**, 157 (1997).
[33]M. A. Mohammad, T. Fito, J. Chen, S. Buswell, M. Aktary, M. Stepanova, and S. K. Dew, Microelectron. Eng. **87**, 1104 (2010).
[34]M. A. Mohammad, T. Fito, J. Chen, S. Buswell, M. Aktary, S. K. Dew, and M. Stepanova, in *Lithography*, edited by Michael Wang (INTECH, Vukovar, Croatia, 2010), pp. 293–318.
[35]B. Wu and A. R. Neureuther, J. Vac. Sci. Technol. B **19**, 2508 (2001).
[36]S. M. Scheinhardt-Engels, F. A. M. Leermakers, and G. J. Fleer, Phys. Rev. E **68**, 011802 (2003).
[37]Z. Tan, Y. Xia, X. Liu, and M. Zhao, Microelectron. Eng. **77**, 285 (2005).
[38]P.-F. Staub, J. Phys. D **27**, 1533 (1994).
[39]A. Jablonski, J. Gryko, J. Kraaser, and S. Tougaard, Phys. Rev. B **39**, 61 (1989).
[40]Truncation of the yield of scission per monomer at the level of 1 limits the present model to the performance of PMMA as a positive tone resist. Extension of the model to include negative-tone PMMA would require lifting of the truncation of the scission events. In this article, however, only positive tone PMMA is considered, and the truncation is compatible.
[41]E. W. Montroll and R. Simha, J. Chem. Phys. **8**, 721 (1940).
[42]W. Kuhn, Ber. Dtsch. Chem. Ges. B **63**, 1503 (1930).
[43]T. Fito, M. A. Mohammad, Zs. Szabó, J. Chen, M. Aktary, S. K. Dew, and M. Stepanova (unpublished).
[44]P. G. de Gennes, J. Chem. Phys. **55**, 572 (1971); Macromolecules **9**, 587 (1976).
[45]V. A. Harmandaris, V. G. Mavrantzas, D. N. Theodorou, M. Kroger, J. Ramirez, H. C. Ottinger, and D. Vlassopoulos, Macromolecules **36**, 1376 (2003).
[46]M. A. Mohammad, T. Fito, J. Chen, M. Aktary, S. K. Dew, and M. Stepanova, J. Vac. Sci. Technol. B **28**, L1 (2010).
[47]The high exposure dose is required for the reason that cold development (−15 °C) has been used in this example; see also the study of the interdependence of optimum exposure and development conditions in Ref. 33.
[48]M. A. Mohammad, Cz. Guthy, S. Evoy, S. K. Dew, and M. Stepanova, J. Vac. Sci. Technol. B (2010) in press. 10.1116/1.3517683